





## Article

# Phase Transformation and Superstructure Formation in (Ti<sub>0.5</sub>, Mg<sub>0.5</sub>)N Thin Films through High-Temperature Annealing

Mohammad Amin Gharavi, Arnaud le Febvrier , Jun Lu, Grzegorz Greczynski , Björn Alling, Rickard Armiento  and Per Eklund \* 

Department of Physics, Chemistry and Biology (IFM), Linköping University, SE-581 83 Linköping, Sweden; mohammad.amin.gharavi@liu.se (M.A.G.); arnaud.le.febvrier@liu.se (A.L.F.); jun.lu@liu.se (J.L.); grzegorz.greczynski@liu.se (G.G.); bjorn.alling@liu.se (B.A.); rickard.armiento@liu.se (R.A.)

\* Correspondence: per.eklund@liu.se

**Abstract:** (Ti<sub>0.5</sub>, Mg<sub>0.5</sub>)N thin films were synthesized by reactive dc magnetron sputtering from elemental targets onto c-cut sapphire substrates. Characterization by  $\theta$ –2 $\theta$  X-ray diffraction and pole figure measurements shows a rock-salt cubic structure with (111)-oriented growth and a twin-domain structure. The films exhibit an electrical resistivity of 150 m $\Omega$ ·cm, as measured by four-point-probe, and a Seebeck coefficient of  $-25$   $\mu$ V/K. It is shown that high temperature ( $\sim 800$  °C) annealing in a nitrogen atmosphere leads to the formation of a cubic LiTiO<sub>2</sub>-type superstructure as seen by high-resolution scanning transmission electron microscopy. The corresponding phase formation is possibly influenced by oxygen contamination present in the as-deposited films resulting in a cubic superstructure. Density functional theory calculations utilizing the generalized gradient approximation (GGA) functionals show that the LiTiO<sub>2</sub>-type TiMgN<sub>2</sub> structure has a 0.07 eV direct bandgap.

**Keywords:** sputtering; thermoelectrics; titanium nitride; magnesium nitride; ternary nitride



**Citation:** Gharavi, M.A.; le Febvrier, A.; Lu, J.; Greczynski, G.; Alling, B.; Armiento, R.; Eklund, P. Phase Transformation and Superstructure Formation in (Ti<sub>0.5</sub>, Mg<sub>0.5</sub>)N Thin Films through High-Temperature Annealing. *Coatings* **2021**, *11*, 89. <https://doi.org/10.3390/coatings11010089>

Received: 10 December 2020

Accepted: 12 January 2021

Published: 14 January 2021

**Publisher's Note:** MDPI stays neutral with regard to jurisdictional claims in published maps and institutional affiliations.



**Copyright:** © 2021 by the authors. Licensee MDPI, Basel, Switzerland. This article is an open access article distributed under the terms and conditions of the Creative Commons Attribution (CC BY) license (<https://creativecommons.org/licenses/by/4.0/>).

## 1. Introduction

Titanium nitride-based hard coatings [1–3] have a long history for use in applications such as protective layers and hard coatings. Thus, the search for TiN based alloys has led to the development of an extensive series of alloys, e.g., Ti–Si–N [4,5] and Ti–Al–N [6–8]. Among the many TiN-based compounds, titanium-magnesium nitride (Ti<sub>0.5</sub>, Mg<sub>0.5</sub>)N [9–11] is of particular interest due to its semiconducting properties, which motivates research on electronic and energy-related applications. Previous attempts to synthesize (Ti<sub>1–x</sub>, Mg<sub>x</sub>)N [12–17] aimed at studying (Ti<sub>1–x</sub>, Mg<sub>x</sub>)N growth and properties, such as oxidation resistance in comparison to pure TiN or use as a decorative coating due to color variations. However, research in (Ti<sub>1–x</sub>, Mg<sub>x</sub>)N alloys gained additional interest due to the research regarding the thermoelectric properties of rock-salt cubic scandium nitride (ScN).

ScN [18–22] exhibits a relatively large thermoelectric power factor of  $(2.5\text{--}3.5) \times 10^{-3}$  Wm<sup>−1</sup>·K<sup>−2</sup>. However, the relatively high thermal conductivity [23–26] of approximately 8–12 Wm<sup>−1</sup>·K<sup>−1</sup> results in a low thermoelectric figure of merit (zT). To address this issue, Alling [27] studied (Ti<sub>1–x</sub>, Mg<sub>x</sub>)N alloys and a hypothetical semiconducting TiMgN<sub>2</sub> superstructure using density functional theory (DFT) and proposed that by replacing the group-3 element scandium with a group-2 alkaline earth element (magnesium) and a group-4 transition metal (titanium), it is possible that the resulting compound will have a similar power factor to that of ScN, but with a reduced thermal conductivity. The study predicted the stability of a naturally layered B1–L1<sub>1</sub> superstructure TiMgN<sub>2</sub>, and that the possible reduced thermal conductivity may stem from interface phonon scattering. The Kohn–Sham band structure calculations predicted stoichiometric TiMgN<sub>2</sub> to have a 1.11 eV bandgap using the HSE06 [28] hybrid functional. Irokawa and Usami [29] predicted similar results using the generalized gradient approximation (GGA) for predicting the

band-structure using Perdew-Burke-Ernzerhof (PBE) functional, [30] which is qualitatively accurate in predicting the existence of band-structure energy gaps.

In a previous paper [31], we studied different crystal structures with an  $ABN_2$  stoichiometry (A and B being elements), concluding that stoichiometric and elementally pure  $TiMgN_2$  is stable in the  $NaCrS_2$  superstructure (which is equivalent to the  $B1-L1_1$  depending on viewpoint direction) and predicted its thermoelectric power factor to be larger compared to  $ScN$ . Furthermore,  $ZrMgN_2$  and  $HfMgN_2$  were also predicted to be thermoelectric semiconductors that may crystallize in either the hexagonal  $NaCrS_2$  superstructure or the  $LiUN_2$  prototype monoclinic structure. These compounds were all predicted to be thermodynamically stable, suggesting that they can be synthesized by physical vapor deposition. Synthesis of  $Mg_xZr_{2-x}N_2$  by Bauers et al. [32] confirms semiconducting properties through temperature-activated conductivity measurements and an onset in the optical absorption spectrum.

Here, we synthesized  $(Ti_{0.5}, Mg_{0.5})N$  thin film alloys and annealed them at high temperatures in a pure nitrogen gas flow. In addition to studying  $(Ti_{0.5}, Mg_{0.5})N$  and its thermoelectric properties, post-annealed  $(Ti_{0.5}, Mg_{0.5})N$  are investigated for the formation of any superstructure and/or other secondary phases.

## 2. Materials and Methods

Depositions were performed by reactive dc magnetron sputtering in an ultra-high vacuum chamber [33]. The films were deposited onto (0001) sapphire substrates ( $10\text{ mm} \times 10\text{ mm} \times 0.5\text{ mm}$ ), ultrasonically cleaned with commercially available detergents (3 min), de-ionized water, acetone and ethanol (10 min each) and blown dry using  $N_2$ . The details of the cleaning method and detergent can be found elsewhere [34]. The substrates were heated  $400\text{ }^\circ\text{C}$  for one hour prior to the deposition process; the temperature was maintained until the end of the process. The films were deposited using 5-cm-diameter Ti (99.95% pure, Kurt J. Lesker, East Sussex, UK) and Mg (99.95% pure, MaTeck, Jülich, Germany) targets and an argon/nitrogen gas mixture (99.9997% pure for both gases). The deposition pressure was set to 0.65 Pa (4.9 mTorr). The substrate holder was rotated with a speed of 15 rpm and at floating potential. The deposition time was 120 min for the 28% nitrogen gas mixture (25 sccm  $N_2$ , 65 sccm Ar).

Most of the characterization approach is analogous to our previous work [35]. X-ray diffraction (XRD)  $\theta$ – $2\theta$  scans were measured in a PANalytical X'Pert PRO diffractometer system (Cu  $K\alpha$ ) (Malvern Panalytical, Almelo, The Netherlands) operated at 45 kV and 40 mA. The incident optics was a Bragg-Brentano module including a  $0.5^\circ$  divergence slit and a  $0.5^\circ$  anti-scatter slit, and the diffracted optics included a 5.0 mm anti-scatter slit and 0.04 rad Soller slits. The solid-state detector was set to one dimensional scanning line mode. Step sizes and collection times per step of  $0.004^\circ$  and 2 s, respectively. Pole figures were acquired in a PANalytical EMPYREAN diffractometer (point focus mode, 45 kV and 40 mA, Malvern Panalytical, Almelo, The Netherlands). A  $2\text{ mm} \times 2\text{ mm}$  crossed slit X-ray lens and a parallel plate collimator as the incident and diffracted beam optics was used, respectively. Pole figures of the  $(Ti_{0.5}, Mg_{0.5})N$  111 peak were acquired for the tilt-angle ( $\psi$ ) range from  $0^\circ$  to  $85^\circ$  and azimuth-angle ( $\varphi$ ) range between  $0^\circ$  and  $360^\circ$  with steps of  $5^\circ$  for both  $\psi$  and  $\varphi$  and a collection time of 1 s.

The chemical composition of the film annealed at  $820\text{ }^\circ\text{C}$  was determined from X-ray photoelectron spectroscopy (XPS, Axis Ultra DLD, Kratos Analytical, Manchester, UK) equipped with a monochromatic Al  $K\alpha$  X-ray radiation ( $h\nu = 1486.6\text{ eV}$ ) source. The base pressure in the analysis chamber during acquisition was less than  $1 \times 10^{-9}$  mbar. Survey spectra and core-level spectra of the Ti 2p, N 1s, Mg 1s, and O 1s regions were recorded as a function of sputter etch time up to 120 min. For that, a 0.5 keV  $Ar^+$  ion beam with an incidence angle of  $20^\circ$  from the surface and rastered over an area of  $3\text{ mm} \times 3\text{ mm}$  was used. Charge compensation was necessary to employ during measurements due to non-conducting substrates. The core-level spectra recorded after  $Ar^+$  etching was used to extract the chemical composition of the film. Here, a Shirley-type background was

subtracted, and elemental cross sections provided by Kratos Analytical were applied. Due to preferential sputtering of nitrogen, a 5% error bar is expected [36].

Scanning electron microscopy (SEM) was performed in a LEO 1550 Gemini SEM (Zeiss, Oberkochen, Germany) operated at 5 kV acceleration voltage. The metal-to-atom ratio was determined by an energy dispersive X-ray spectroscopy (EDS, Oxford Instruments, Abingdon, UK) setup with the acceleration voltage set to 20 kV. High resolution-scanning transmission electron microscopy (HR-STEM) was performed in a Titan<sup>3</sup> 60–300 (FEI, Hillsboro, OR, USA). An FEI Tecnai G2 TF20 (Hillsboro, OR, USA) with a field-emission gun operating at 200 kV was used for selected area electron diffraction (SAED). Cross-sectional samples for the TEM were prepared by mechanical polishing to ~55  $\mu\text{m}$  by hand. Ion milling was then performed using a Precision Ion Polishing System (PIPS, Gatan, Pleasanton, CA, USA) with a 5 keV  $\text{Ar}^+$  ion beam, angle of incidence  $8^\circ$  relative to the sample surface for 2 h, and  $5^\circ$  for 4 h. Once electron transparency was reached, a final ion milling step was applied with lower energy ion beams (2 keV) for 30 min.

The electrical resistivity of all samples was obtained by measuring the sheet resistance of the films with a four-point-probe RM3000 station (Jandel, Leighton Buzzard, UK). The measured sheet resistance was multiplied with the film thickness of approximately 250 nm (from cross-section SEM,  $\pm 10$  nm) to obtain the resistivity. The Seebeck coefficient was obtained by an in-house setup described elsewhere [37]. Measurements were conducted in open-air conditions and the temperature gradient over the sample was approximately  $50^\circ\text{C}$ . Sample annealing was done in an air-tight furnace with a nitrogen gas flow. Each annealing session was done for 30 min at 610, 770, and  $820^\circ\text{C}$ . A final annealing session at  $820^\circ\text{C}$  was also done for 1 h.

Density functional theory calculations were performed to study the electronic band structure of a  $\text{LiTiO}_2$ -type ( $\text{I4}_1/\text{amd}$ )  $\text{TiMgN}_2$  structure. First-principles calculations were performed using DFT [38,39] with the projector augmented wave method (PAW) [40] as implemented in the Vienna ab initio simulation package (VASP) [41–43] version 5.2. Electronic exchange-correlation effects and the electronic band structure were modeled with the generalized gradient approximation (GGA) using the Perdew-Burke-Ernzerhof (PBE) functional [30]. The Kohn-Sham gaps of standard GGA calculations are systematically smaller than experimental bandgaps, but the results are suitable for qualitative research. The plane wave energy cutoff was set at 600 eV. The required structure files for the crystal structures were obtained from the Inorganic Crystal Structure Database (ICSD) and converted to VASP input files using cif2cell [44]. The band structure illustrations were prepared by the high-throughput toolkit (httk) [45], and the crystal structures by Visualization for Electronic and Structural Analysis (VESTA) [46].

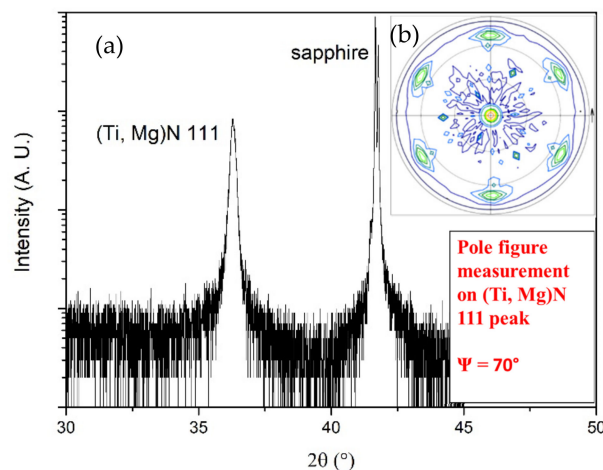
The present work uses the same correction of the  $\text{N}_2$  energy as used in the Materials Project, based on work by Wang et al. [47]. It is known that standard GGA exchange-correlation functionals in DFT, have systematic errors in the prediction of energy differences between solid and gas phase systems [48]. Hence, it is common to adjust the gas phase energy in order to reproduce the formation energy of a system relative to a gas end-point.

The calculations used a  $4 \times 4 \times 4$  k-point mesh for Brillouin zone sampling generated with the Monkhorst-Pack scheme [49]. For band structure calculations, the tetrahedron method was used to obtain bandgap values with spin polarization included [50].

### 3. Result and Discussion

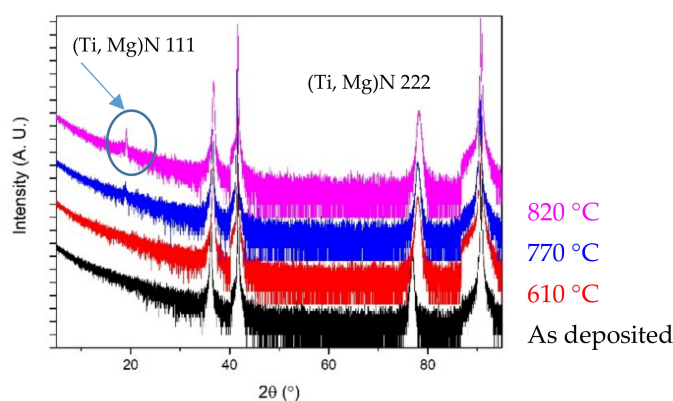
Figure 1 shows a  $\theta$ – $2\theta$  scan of a  $(\text{Ti}_{0.5}, \text{Mg}_{0.5})\text{N}$  random alloy as-deposited film on a c-cut sapphire substrate. The 111 peak from a face-centered cubic TiN structure of the film is observed next to the sapphire 0006 substrate peak. The inset shows a pole figure measurement of the  $(\text{Ti}_{0.5}, \text{Mg}_{0.5})\text{N}$  thin film. The pole figure is performed at  $2\theta = 36.30^\circ$  corresponding to diffraction from the (111) lattice plane. In this case, six high-intensity poles at  $\psi = 70^\circ$  surround the center pole due to twin-domain growth which is expected for the growth of a cubic material on sapphire substrates. Based on the peak position, the lattice parameter for  $(\text{Ti}_{0.5}, \text{Mg}_{0.5})\text{N}$  is approximately  $a_0 = 4.30 \text{ \AA}$ . Assuming the theoretical

lattice parameter of 4.44 Å for  $\text{MgN}^{50}$ , 4.25 Å for TiN (Materials Project database) and Vegard's law for a 50–50 random alloy, the theoretical lattice parameter value for  $(\text{Ti}_{0.5}, \text{Mg}_{0.5})\text{N}$  would be approximately 4.35 Å.



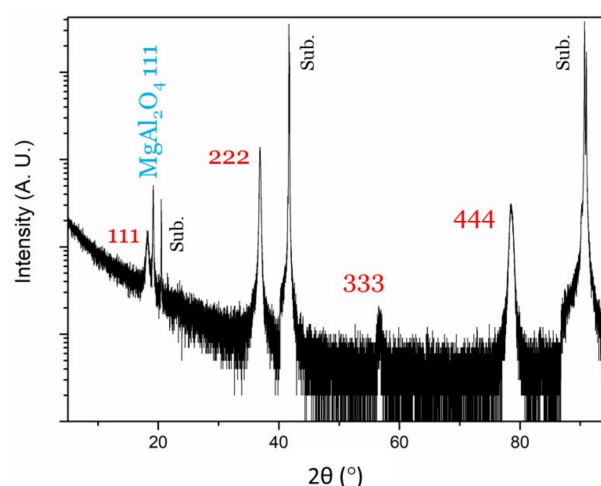
**Figure 1.** (a) XRD of as-deposited  $(\text{Ti}_{0.5}, \text{Mg}_{0.5})\text{N}$  thin film showing growth in the (111) direction; (b) Pole figure measurements (inset) show twin-domain epitaxial growth.

Figure 2 shows the post-annealing  $\theta$ – $2\theta$  scans of a  $(\text{Ti}_{0.5}, \text{Mg}_{0.5})\text{N}$  film after 30 min of heat treatment in pure nitrogen. After annealing at 610 °C, the 111 peak shows a shift towards a larger  $2\theta$  angle, presumably resulting from stress relaxation in the film. However, after annealing at 770 °C, a small peak located at  $2\theta \sim 19^\circ$  shows the presence of a phase with a relatively large lattice parameter. After annealing at 820 °C, this peak becomes more pronounced (marked by an arrow in Figure 2).



**Figure 2.** XRD comparison between as-deposited  $(\text{Ti}_{0.5}, \text{Mg}_{0.5})\text{N}$  film with post-annealed films (30 min duration). At 820 °C, phase transformation becomes evident.

In order to further develop the phase transformation seen in Figure 2, the film was then annealed for an additional hour at 820 °C, yielding a set of more pronounced XRD peaks located at  $2\theta = 18.25^\circ, 36.88^\circ, 56.75^\circ$ , and  $78.53^\circ$  seen in Figure 3. These peaks are multiples of each other (Table 1). The additional peak located at  $2\theta = 19.18^\circ$  originates from a spinel phase,  $\text{MgAl}_2\text{O}_4$ , most likely formed by a reaction between the film and the substrate [51].



**Figure 3.** XRD of post-annealed  $(\text{Ti}_{0.5}, \text{Mg}_{0.5})\text{N}$  thin film (60 min duration). The results show the evolution of new peaks pointing towards a phase transformation and includes a reaction between the film and substrate ( $\text{MgAl}_2\text{O}_4$  111).

**Table 1.** Relationship between peaks of post-annealed  $(\text{Ti}_{0.5}, \text{Mg}_{0.5})\text{N}$  thin film (60 min duration). Results show that the newly formed peaks are multiples of each other.

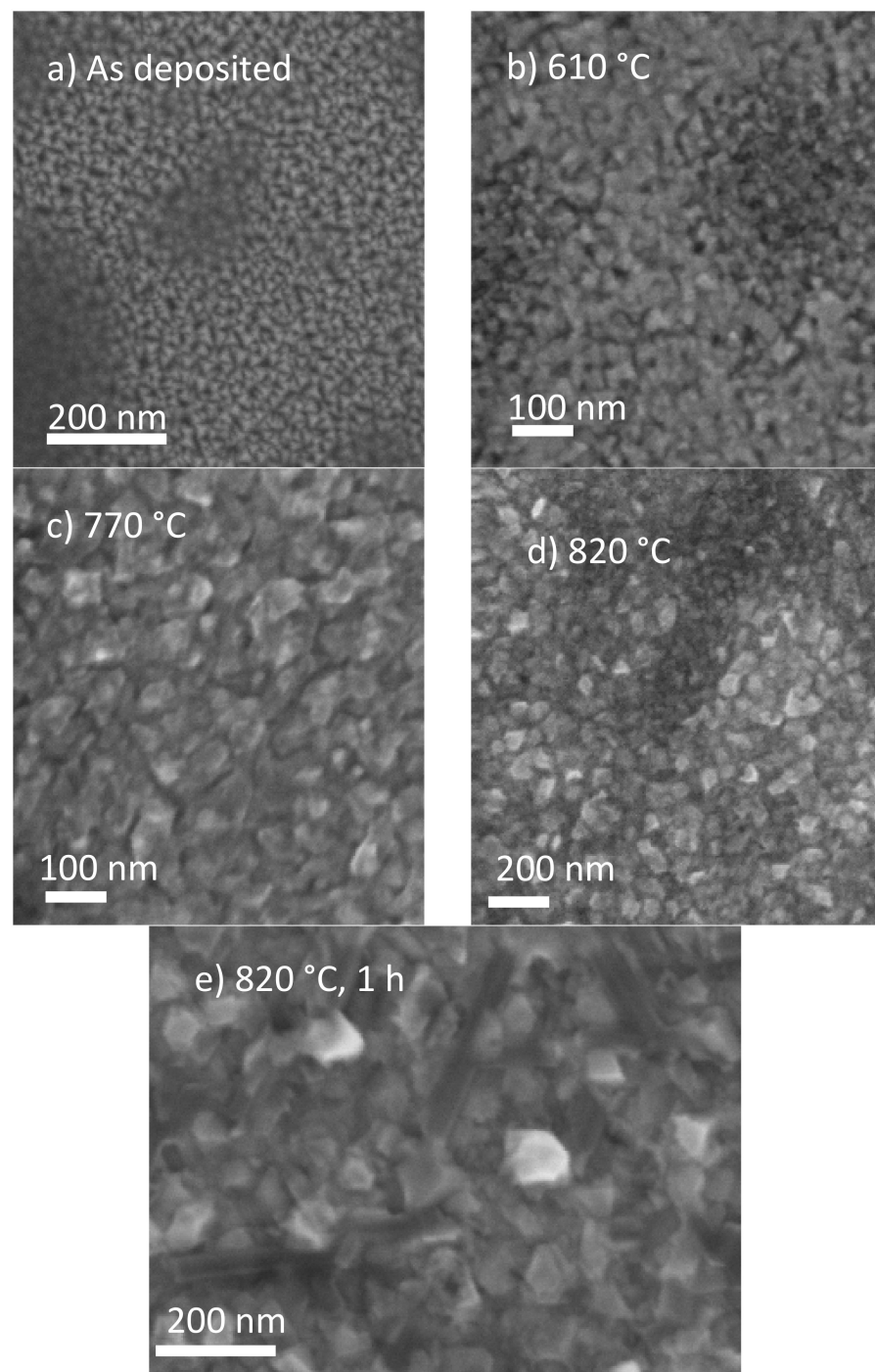
$2\theta$ (°)	d-Spacing (Å)	Multiple
18.25	4.86	1
36.88	2.44	1/2
56.75	1.62	1/3
78.53	1.22	1/4

Figure 4a shows an SEM image of the as-deposited film surface. The film is porous and has a columnar-type growth, consistent with the relatively low deposition temperature of 400 °C, which was chosen due to the relatively high vapor pressure of magnesium. EDS measurements show that the as-deposited  $(\text{Ti}_{0.5}, \text{Mg}_{0.5})\text{N}$  film has a 1:1 Ti/Mg atom ratio. The room-temperature in-plane electrical resistivity of the as-deposited film is measured to be 150 mΩ·cm, several orders of magnitude higher than pure TiN (20 μΩ·cm [52]). This is due to the addition of magnesium, consistent with the fact that magnesium nitride is a semiconductor. Note that magnesium nitride has the  $\text{Mg}_3\text{N}_2$  stoichiometry, and that the stabilized mononitride MgN (due to the TiN structure) would be highly prone to oxidation in pure form. The room-temperature Seebeck coefficient is measured to be approximately −25 μV/K, lower but of the same order of magnitude as ScN.

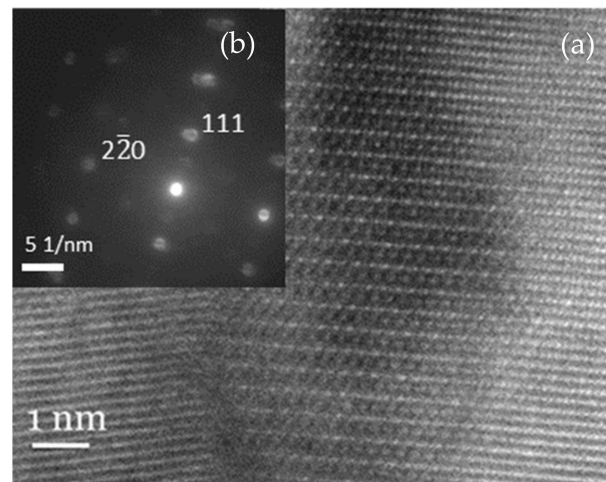
Figure 4b–d show SEM images of the surface morphology after annealing, showing a major change in the surface morphology. Further annealing of the sample for one hour at 820 °C fully transforms the surface morphology from the initial columnar growth, as seen in Figure 4e.

Figure 5 shows a Z-contrast high-resolution scanning transmission electron microscopy (HR-STEM) image of the  $(\text{Ti}_{0.5}, \text{Mg}_{0.5})\text{N}$  film annealed at 820 °C for one hour. The image shows a 5 nm × 10 nm nanoinclusion superstructure inside the  $(\text{Ti}_{0.5}, \text{Mg}_{0.5})\text{N}$  rock-salt cubic matrix and positioned in between grain boundaries. The inset in Figure 5 shows the selected area electron diffraction (SAED) of the nanoinclusion showing a cubic structure along the  $[11\bar{2}]$  direction. However, these nanoinclusions have a lattice constant twice as large compared to the rock-salt  $(\text{Ti}_{0.5}, \text{Mg}_{0.5})\text{N}$  alloy, and form as an ordered superstructure on the same underlying lattice after the temperature-activated phase transformation.





**Figure 4.** SEM comparison between as-deposited  $(\text{Ti}_{0.5}, \text{Mg}_{0.5})\text{N}$  film with post-annealed films. The as-deposited films show a porous and columnar-type growth, while as the post-annealed films show a change in surface morphology hinting towards surface oxidation: (a) as-deposited; (b) annealed at 610 °C; (c) annealed at 770 °C; (d) annealed at 820 °C; (e) annealed at 820 °C for one hour.



**Figure 5.** (a) High-resolution STEM image of newly formed nanoinclusions. Note that phase transformation occurs at grain boundaries; (b) SAED image of the nanoinclusion.

An XPS depth profile (Figure 6) was performed on the  $(\text{Ti}_{0.5}\text{Mg}_{0.5})\text{N}$  alloy film (annealed at 820 °C) to study oxidation effects. The results show that this annealed sample is highly inhomogeneous. Mg and O are the only elements present at the surface and the quantitative analysis suggests stoichiometric MgO formation. This could explain the surface morphology change seen in Figure 4, indicating continued oxidation during annealing processes. The porous features of the as-deposited film are most likely the source of the oxygen in the film when removing it from the UHV chamber. After prolonged sputter-etching, the film consists of approximately 24 at.% titanium, 21 at.% nitrogen, 19 at.% magnesium and 36 at.% oxygen. Due to the lack of an internal charge reference, the reliable determination of the bonding character cannot be attempted [53]. Nevertheless, the Ti 2p spectrum shows that Ti atoms are present in multiple chemical states likely involving Ti–N, Ti–O<sub>x</sub>–N<sub>y</sub>, and Ti–O bonding. EDS measurements (Figure 7) shows that the post-annealed film consists of titanium-rich and magnesium-rich regions (~10 nm in size) with a nanometer-sized boundary layer in between. These results, coupled with the HR-STEM, show that the phase transformation initially identified by XRD is due to Ti/Mg oxynitride nanoinclusions that form in between grain boundaries. These nanoinclusions show a similar structure to that of the LiTiO<sub>2</sub>-type cubic structure [54] (Figure 8, top image) and hint towards TiMgN<sub>2</sub> formation being oxidized during the annealing process due to the initial presence of oxygen in the porous film. The predicted structure has an  $a = b = c = 8.635 \text{ \AA}$  lattice parameter at  $\alpha = \beta = \gamma = 90^\circ$  and a unit cell volume of approximately  $644 \text{ \AA}^3$  (Niggli-reduced cell:  $a = b = c = 6.106 \text{ \AA}$  and  $\alpha = \beta = \gamma = 60^\circ$ ). Note that the electron count for phase pure LiTiO<sub>2</sub> ( $\text{Li}^{1+} \text{Ti}^{4+} \text{O}^{2-} \text{O}^{2-}$ ) is +1, and thus it would not be a semiconductor, although DFT calculations of TiMgN<sub>2</sub> crystallized in the LiTiO<sub>2</sub>-type cubic structure predicts an electronic band structure (Figure 8, bottom image) with a 0.07 eV direct bandgap. The predicted band structure uses the PBE GGA functional, which systematically gives Kohn-Sham bandgaps that are smaller than experimentally observed gaps. This means that since we find the existence of a bandgap in our calculations, the material would, if existing, display an even larger gap.

It should be noted that neither the NaCrS<sub>2</sub> nor the LiUN<sub>2</sub> structures regarding the hypothetical TiMgN<sub>2</sub> structure are observed experimentally here. This could be explained by the oxygen present in the film which may drive the phase transformation towards a cubic superstructure. Also, it is possible that a cubic superstructure is preferred over the layered NaCrS<sub>2</sub> structure when the starting crystal structure is rock-salt cubic.

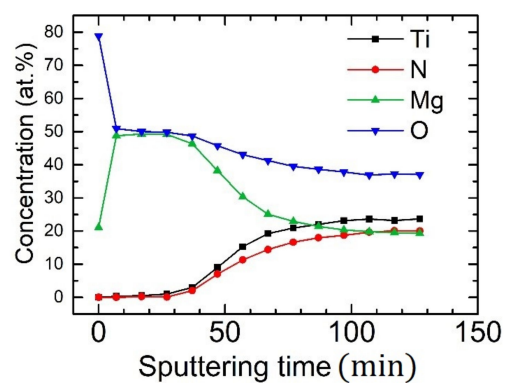


**Figure 6.** XPS depth profile of the  $(\text{Ti}_{0.5}, \text{Mg}_{0.5})\text{N}$  alloy film (annealed at  $820^\circ\text{C}$ ).

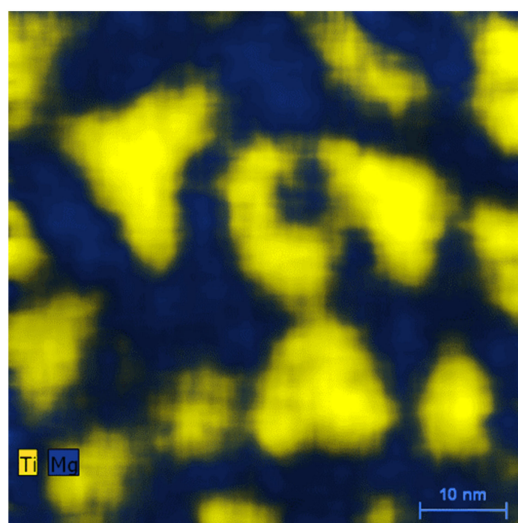


**Figure 7.** EDS map of post-annealed film shows magnesium-rich and titanium-rich regions with phase transformation occurring in between.

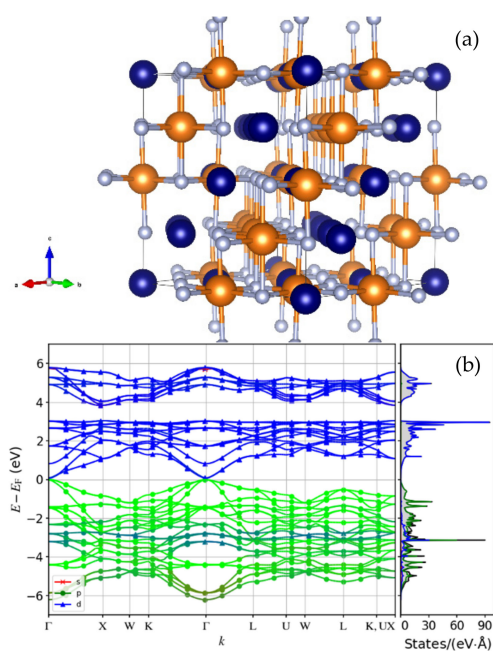


**Figure 8.** (a) 3D rendering of the  $\text{LiTiO}_2$ -type stoichiometric  $\text{TiMgN}_2$  structure; (b) DFT band structure calculations predict that  $\text{LiTiO}_2$ -type  $\text{TiMgN}_2$  has a direct bandgap of 0.07 eV.



#### 4. Conclusions

(Ti<sub>0.5</sub>, Mg<sub>0.5</sub>)N thin films with a 1:1 metallic atom ratio were synthesized by reactive magnetron sputter deposition onto c-cut sapphire substrates. (Ti<sub>0.5</sub>, Mg<sub>0.5</sub>)N is a semiconductor, and exhibits a Seebeck coefficient value of a  $-25 \mu\text{V/K}$  and an electrical resistivity of  $150 \text{ m}\Omega\cdot\text{cm}$  at room temperature. Thermal annealing of (Ti<sub>0.5</sub>, Mg<sub>0.5</sub>)N results in the formation of a cubic superstructure in the form of a LiTiO<sub>2</sub>-type nanoinclusion inside the rock-salt cubic solid solution. Due to the presence of oxygen in the film, the nanoinclusions are a Ti/Mg-based oxynitride; such a quaternary phase may show interesting semiconducting properties. DFT calculations for a stoichiometric TiMgN<sub>2</sub> crystallized in the LiTiO<sub>2</sub> structure predict that this superstructure has a direct bandgap of 0.07 eV. It is possible that a Ti/Mg oxynitride with semiconducting properties would show high oxidation resistance, making it a suitable choice for research regarding high-temperature applications (e.g., thermoelectrics). Additional research could also focus on the synthesis and annealing of denser and oxygen-free thin films, preferably at higher temperatures.

**Author Contributions:** Conceptualization, M.A.G., R.A., B.A., and P.E.; formal analysis, M.A.G., A.I.F., J.L., G.G., R.A., B.A., and P.E.; investigation, M.A.G., A.I.F., J.L., G.G., R.A., B.A., and P.E.; writing—original draft preparation, M.A.G.; writing—review and editing, A.I.F., J.L., G.G., R.A., B.A., and P.E.; supervision, R.A., B.A., and P.E.; funding acquisition, R.A., B.A., and P.E. All authors have read and agreed to the published version of the manuscript.

**Funding:** The authors acknowledge funding from the Swedish Government Strategic Research Area in Materials Science on Functional Materials at Linköping University (Faculty Grant SFO-Mat-LiU No. 2009 00971), the Knut and Alice Wallenberg foundation through the Wallenberg Academy Fellows program (P.E.) KAW-2020.0196 and Wallenberg Scholar Grant No. KAW-2018.0194, and the Swedish Research Council (VR) under project No. 2016-03365 and No. 2019-05403. B.A. also acknowledges support from the Swedish Foundation for Strategic Research through the Future Research Leaders 6 program, FFL 15-0290. The computations were enabled by resources provided by the Swedish National Infrastructure for Computing (SNIC) at NSC partially funded by the Swedish Research Council through grant agreement No. 2018-05973.

**Institutional Review Board Statement:** Not applicable.

**Informed Consent Statement:** Not applicable.

**Data Availability Statement:** Data is contained within the article or available on reasonable request.

**Conflicts of Interest:** The authors declare no conflict of interest.

#### References

1. Sundgren, J.-E. Structure and properties of TiN coatings. *Thin Solid Films* **1985**, *128*, 21–44. [\[CrossRef\]](#)
2. Hultman, L. Thermal stability of nitride thin films. *Vacuum* **2000**, *57*, 1–30. [\[CrossRef\]](#)
3. Mayrhofer, P.H.; Mitterer, C.; Hultman, L.; Clemens, H. Microstructural design of hard coatings. *Prog. Mater. Sci.* **2006**, *51*, 1032–1114. [\[CrossRef\]](#)
4. Hultman, L.; Bareno, J.; Flink, A.; Söderberg, H.; Larsson, K.; Petrova, V.; Odén, M.; Greene, J.E.; Petrov, I. Interface structure in superhard TiN–SiN nanolaminates and nanocomposites: Film growth experiments and ab initio calculations. *Phys. Rev. B* **2007**, *75*, 155437. [\[CrossRef\]](#)
5. Diserens, M.; Patscheider, J.; Lévy, F. Improving the properties of titanium nitride by incorporation of silicon. *Surf. Coat. Technol.* **1998**, *108–109*, 241–246. [\[CrossRef\]](#)
6. Münz, W.-D. Titanium aluminum nitride films: A new alternative to TiN coatings. *J. Vac. Sci. Technol. A* **1986**, *4*, 2717. [\[CrossRef\]](#)
7. Leyendecker, T.; Lemmer, O.; Esser, S.; Ebberink, J. The development of the PVD coating TiAlN as a commercial coating for cutting tools. *Surf. Coat. Technol.* **1991**, *48*, 175–178. [\[CrossRef\]](#)
8. Hörling, A.; Hultman, L.; Odén, M.; Sjöln, J.; Karlsson, L. Mechanical properties and machining performance of Ti<sub>1-x</sub>Al<sub>x</sub>N-coated cutting tools. *Surf. Coat. Technol.* **2005**, *191*, 384–392. [\[CrossRef\]](#)
9. Wang, B.; Kerdsonpanya, S.; McGahay, M.E.; Milosevic, E.; Patsalas, P.; Gall, D. Growth and properties of epitaxial Ti<sub>1-x</sub>Mg<sub>x</sub>N(001) layers. *J. Vac. Sci. Technol. A* **2018**, *36*, 061501. [\[CrossRef\]](#)
10. Baiwei, B.; Gall, D. A new semiconductor: Ti<sub>0.5</sub>Mg<sub>0.5</sub>N(001). In Proceedings of the 2018 IEEE Nanotechnology Symposium (ANTS), Albany, NY, USA, 14–15 November 2018.
11. Sun, W.; Bartel, C.J.; Arca, E.; Bauers, S.R.; Matthews, B.; Orvañanos, B.; Chen, B.-R.; Toney, M.F.; Schelhas, L.T.; Tumas, W.; et al. A map of the inorganic ternary metal nitrides. *Nat. Mater.* **2019**, *18*, 732–739. [\[CrossRef\]](#)

12. Banakh, O.; Balzer, M.; Fenker, M.; Blatter, A. Spectroellipsometric evaluation of colour and oxidation resistance of TiMgN coatings. *Thin Solid Films* **2004**, *455–456*, 650–655. [\[CrossRef\]](#)
13. Fenker, M.; Balzer, M.; Kappl, H.; Banakh, O. Some properties of (Ti,Mg)N thin films deposited by reactive dc magnetron sputtering. *Surf. Coat. Technol.* **2005**, *200*, 227–231. [\[CrossRef\]](#)
14. Fenker, M.; Balzer, M.; Kappl, H. Corrosion behaviour of decorative and wear resistant coatings on steel deposited by reactive magnetron sputtering—Tests and improvements. *Thin Solid Films* **2006**, *515*, 27–32. [\[CrossRef\]](#)
15. Hodroj, A.; Chaix-Pluchery, O.; Steyer, P.; Pierson, J.F. Oxidation resistance of decorative (Ti,Mg)N coatings deposited by hybrid cathodic arc evaporation-magnetron sputtering process. *Surf. Coat. Technol.* **2011**, *205*, 4547–4553. [\[CrossRef\]](#)
16. Onder, S.; Kok, F.N.; Kazmanli, K.; Urgen, M. Magnesium substituted hydroxyapatite formation on (Ti,Mg)N coatings produced by cathodic arc PVD technique. *Mater. Sci. Eng. C* **2013**, *33*, 4337–4342. [\[CrossRef\]](#) [\[PubMed\]](#)
17. Wang, B.; Gall, D. Fully strained epitaxial  $\text{Ti}_{1-x}\text{Mg}_x\text{N}$  (001) layers. *Thin Solid Films* **2019**, *688*, 137165. [\[CrossRef\]](#)
18. Eklund, P.; Kerdsonpanya, S.; Alling, B. Transition-metal-nitride-based thin films as novel energy harvesting materials. *J. Mater. Chem. C* **2016**, *4*, 3905–3914. [\[CrossRef\]](#)
19. Kerdsonpanya, S.; Nong, N.V.; Pryds, N.; Žukauskaitė, A.; Jensen, J.; Birch, J.; Lu, J.; Hultman, L.; Wingqvist, G.; Eklund, P. Anomalous high thermoelectric power factor in epitaxial ScN thin films. *Appl. Phys. Lett.* **2011**, *99*, 232113. [\[CrossRef\]](#)
20. Burmistrova, P.V.; Zakharov, D.N.; Favaloro, T.; Mohammed, A.; Stach, E.A.; Shakouri, A.; Sands, T.D. Effect of deposition pressure on the microstructure and thermoelectric properties of epitaxial ScN(001) thin films sputtered onto MgO(001) substrates. *J. Mater. Res.* **2015**, *30*, 626–634. [\[CrossRef\]](#)
21. Tureson, N.; Marteau, M.; Cabioch, T.; Nong, N.V.; Jensen, J.; Lu, J.; Greczynski, G.; Fournier, D.; Singh, N.; Soni, A.; et al. Effect of ion-implantation-induced defects and Mg dopants on the thermoelectric properties of ScN. *Phys. Rev. B* **2018**, *98*, 205307. [\[CrossRef\]](#)
22. Biswas, B.; Saha, B. Development of semiconducting ScN. *Phys. Rev. Mater.* **2019**, *3*, 020301. [\[CrossRef\]](#)
23. Burmistrova, P.V.; Maassen, J.; Favaloro, T.; Saha, B.; Salamat, S.; Koh, Y.R.; Lundstrom, M.S.; Shakouri, A.; Sands, T.D. Thermoelectric properties of epitaxial ScN films deposited by reactive magnetron sputtering onto MgO(001) substrates. *J. Appl. Phys.* **2013**, *113*, 153704. [\[CrossRef\]](#)
24. King, S.W.; Davis, R.F.; Nemanich, R.J. Gas source molecular beam epitaxy of scandium nitride on silicon carbide and gallium nitride surfaces. *J. Vac. Sci. Technol. A* **2014**, *32*, 061504. [\[CrossRef\]](#)
25. Kerdsonpanya, S.; Sun, B.; Eriksson, F.; Jensen, J.; Lu, J.; Koh, Y.K.; Nong, N.V.; Balke, B.; Alling, B.; Eklund, P. Experimental and theoretical investigation of  $\text{Cr}_{1-x}\text{Sc}_x\text{N}$  solid solutions for thermoelectrics. *J. Appl. Phys.* **2016**, *120*, 215103. [\[CrossRef\]](#)
26. Kerdsonpanya, S.; Hellman, O.; Sun, B.; Koh, Y.K.; Lu, J.; Nong, N.V.; Simak, S.I.; Alling, B.; Eklund, P. Phonon thermal conductivity of scandium nitride for thermoelectrics from first-principles calculations and thin-film growth. *Phys. Rev. B* **2017**, *96*, 195417. [\[CrossRef\]](#)
27. Alling, B. Metal to semiconductor transition and phase stability of  $\text{Ti}_{1-x}\text{Mg}_x\text{N}_y$  alloys investigated by first-principles calculations. *Phys. Rev. B* **2014**, *89*, 085112. [\[CrossRef\]](#)
28. Heyd, J.; Scuseria, G.E.; Ernzerhof, M. Hybrid functionals based on a screened Coulomb potential. *J. Chem. Phys.* **2003**, *118*, 8207–8215. [\[CrossRef\]](#)
29. Irokawa, Y.; Usami, M. First-principles calculations of semiconducting  $\text{TiMgN}_2$ . *Jpn. J. Appl. Phys.* **2016**, *55*, 098001. [\[CrossRef\]](#)
30. Perdew, J.P.; Burke, K.; Ernzerhof, M. Generalized gradient approximation made simple. *Phys. Rev. Lett.* **1996**, *77*, 3865–3868. [\[CrossRef\]](#)
31. Gharavi, M.A.; Armiento, R.; Alling, B.; Eklund, P. Theoretical study of phase stability, crystal and electronic structure of  $\text{MeMgN}_2$  (Me = Ti, Zr, Hf) compounds. *J. Mater. Sci.* **2018**, *53*, 4294–4305. [\[CrossRef\]](#)
32. Bauers, S.R.; Hamann, D.M.; Patterson, A.; Perkins, J.D.; Talley, K.R.; Zakutayev, A. Composition, structure, and semiconducting properties of  $\text{Mg}_x\text{Zr}_{2-x}\text{N}_2$  thin films. *Jpn. J. Appl. Phys.* **2019**, *58*, SC1015. [\[CrossRef\]](#)
33. Le Febvrier, A.; Landälv, L.; Liersch, T.; Sandmark, D.; Sandström, P.; Eklund, P. An upgraded ultra-high vacuum magnetron-sputtering system for high-versatility and software-controlled deposition. *arXiv* **2020**, arXiv:2010.08411.
34. Le Febvrier, A.; Jensen, J.; Eklund, P. Wet-cleaning of MgO(001): Modification of surface chemistry and effects on thin film growth investigated by X-ray photoelectron spectroscopy and time-of-flight secondary ion mass spectroscopy. *J. Vac. Sci. Technol. A* **2017**, *35*, 021407. [\[CrossRef\]](#)
35. Gharavi, M.A.; Greczynski, G.; Eriksson, F.; Lu, J.; Balke, B.; Fournier, D.; le Febvrier, A.; Pallier, C.; Eklund, P. Synthesis and characterization of single-phase epitaxial  $\text{Cr}_2\text{N}$  thin films by reactive magnetron sputtering. *J. Mater. Sci.* **2019**, *54*, 1434–1442. [\[CrossRef\]](#)
36. Haasch, R.T.; Lee, T.-Y.; Gall, D.; Greene, J.E.; Petrov, I. Epitaxial TiN(001) grown and analyzed in situ by XPS and UPS. II. Analysis of  $\text{Ar}^+$  Sputter Etched Layers. *Surf. Sci. Spectra* **2000**, *7*, 204–212. [\[CrossRef\]](#)
37. Le Febvrier, A.; Tureson, N.; Stillerich, N.; Greczynski, G.; Eklund, P. Effect of impurities on morphology, growth mode, and thermoelectric properties of (111) and (001) epitaxial-like ScN films. *J. Phys. D Appl. Phys.* **2018**, *52*, 035302. [\[CrossRef\]](#)
38. Hohenberg, P.; Kohn, W. Inhomogeneous electron gas. *Phys. Rev.* **1964**, *136*, B864–B871. [\[CrossRef\]](#)
39. Kohn, W.; Sham, L.J. Self-consistent equations including exchange and correlation effects. *Phys. Rev.* **1965**, *140*, A1133–A1138. [\[CrossRef\]](#)
40. Blöchl, P.E. Projector augmented-wave method. *Phys. Rev. B* **1994**, *50*, 17953–17979. [\[CrossRef\]](#)

41. Kresse, G.; Hafner, J. Ab initio molecular dynamics for open-shell transition metals. *Phys. Rev. B* **1993**, *48*, 13115–13118. [[CrossRef](#)]
42. Kresse, G.; Furthmüller, J. Efficient iterative schemes for Ab initio total-energy calculations using a plane-wave basis set. *Phys. Rev. B* **1996**, *54*, 11169–11186. [[CrossRef](#)] [[PubMed](#)]
43. Kresse, G.; Joubert, D. From ultrasoft pseudopotentials to the projector augmented-wave method. *Phys. Rev. B* **1999**, *59*, 1758–1775. [[CrossRef](#)]
44. Björkman, T. CIF2Cell: Generating geometries for electronic structure programs. *Comput. Phys. Commun.* **2011**, *182*, 1183–1186. [[CrossRef](#)]
45. Armiento, R.; Tholander, C.; Björkman, T.; Armiento, R.; Steneteg, P.; Mogyasz, I. The High-Throughput Toolkit (httk). Available online: <http://httk.openmaterialsdb.se/> (accessed on 12 January 2021).
46. Momma, K.; Izumi, F. VESTA 3 for three-dimensional visualization of crystal, volumetric and morphology data. *J. Appl. Crystallogr.* **2011**, *44*, 1272–1276. [[CrossRef](#)]
47. Wang, L.; Maxisch, T.; Ceder, G. Oxidation energies of transition metal oxides within the GGA + U framework. *Phys. Rev. B* **2006**, *73*, 195107. [[CrossRef](#)]
48. Jain, A.; Hautier, G.; Moore, C.J.; Ong, S.P.; Fischer, C.C.; Mueller, T.; Persson, K.A.; Ceder, G. A high-throughput infrastructure for density functional theory calculations. *Comp. Mater. Sci.* **2011**, *50*, 2295–2310. [[CrossRef](#)]
49. Monkhorst, H.J.; Pack, J.D. Special points for Brillouin-zone integrations. *Phys. Rev. B* **1976**, *13*, 5188–5192. [[CrossRef](#)]
50. Droghetti, A.; Baadji, N.; Sanvito, S. MgN: A possible material for spintronic applications. *Phys. Rev. B* **2009**, *80*, 235310. [[CrossRef](#)]
51. Li, J.; Nutt, S.R.; Kirby, K.W. Surface modification of sapphire by magnesium-ion implantation. *J. Am. Ceram. Soc.* **1999**, *82*, 3260–3262. [[CrossRef](#)]
52. Ningthoujam, R.S.; Gajbhiye, N.S. Synthesis, electron transport properties of transition metal nitrides and applications. *Prog. Mater. Sci.* **2015**, *70*, 50–154. [[CrossRef](#)]
53. Greczynski, G.; Hultman, L. Compromising science by ignorant instrument calibration—Need to revisit half a century of published XPS data. *Angew. Chem. Int. Ed.* **2020**, *59*, 5002–5006. [[CrossRef](#)] [[PubMed](#)]
54. Cava, R.J.; Murphy, D.W.; Zahurak, S.M.; Santoro, A.; Roth, R.S. The crystal structures of the lithium-inserted metal oxides  $\text{Li}_{0.5}\text{TiO}_2$  anatase,  $\text{LiTi}_2\text{O}_4$  spinel, and  $\text{Li}_2\text{Ti}_2\text{O}_7$ . *J. Solid State Chem.* **1984**, *53*, 64–75. [[CrossRef](#)]